

# MAVIS: science case, imager and spectrograph

Simon Ellis<sup>a</sup>, Richard McDermid<sup>b</sup>, Giovanni Cresci<sup>d</sup>, Christian Schwab<sup>a,b</sup>, Francois Rigaut<sup>c</sup>, Timothy Chin<sup>a</sup>, Robert Content<sup>a</sup>, Anthony Horton<sup>a</sup>, Mahesh Mohanan<sup>a</sup>, Helen McGregor<sup>a</sup>, Jacob Pember<sup>b</sup>, David Robertson<sup>a</sup>, Lew Waller<sup>a</sup>, Ross Zhelem<sup>a</sup>, Stephanie Monty<sup>c</sup>, Trevor Mendel<sup>c</sup>, Matteo Aliverti<sup>d</sup>, Guido Agapito<sup>d</sup>, Simone Antonucci<sup>d</sup>, Andrea Balestra<sup>d</sup>, Andrea Baruffolo<sup>d</sup>, Maria Bergomi<sup>d</sup>, Andrea Bianco<sup>d</sup>, Marco Bonaglia<sup>d</sup>, Giuseppe Bono<sup>d</sup>, Jean-Claude Bouret<sup>e</sup>, David Brodrick<sup>c</sup>, Lorenzo Busoni<sup>d</sup>, Elena Carolo<sup>d</sup>, Simonetta Chinellato<sup>d</sup>, Jesse Cranney<sup>c</sup>, Gayandhi de Silva<sup>a</sup>, Simone Esposito<sup>d</sup>, Daniela Fantinel<sup>d</sup>, Jacopo Farinato<sup>d</sup>, Thierry Fusco<sup>e,h</sup>, Gaston Gausachs<sup>c</sup>, James Gilbert<sup>c</sup>, Damien Gratadour<sup>c,g</sup>, Davide Greggio<sup>d</sup>, Marco Gullieuszik<sup>d</sup>, Pierre Haguenaue<sup>f</sup>, Dionne Haynes<sup>c</sup>, Visa Korkiakoski<sup>c</sup>, Demetrio Magrin<sup>d</sup>, Laura Magrini<sup>d</sup>, Luca Marafatto<sup>d</sup>, Benoit Neichel<sup>e</sup>, Fernando Pedichini<sup>d</sup>, Enrico Pinna<sup>d</sup>, Cedric Plantet<sup>d</sup>, Elisa Portaluri<sup>d</sup>, Kalyan Radhakrishnan Santhakumari<sup>c</sup>, Roberto Ragazzoni<sup>d</sup>, Bernardo Salasnich<sup>d</sup>, Stefan Ströbele<sup>f</sup>, Elliott Thorn<sup>c</sup>, Annino Vaccarella<sup>c</sup>, Daniele Vassallo<sup>d</sup>, Valentina Viotto<sup>d</sup>, Frédéric Zamkotsian<sup>e</sup>, Alessio Zanutta<sup>d</sup>, and Hao Zhang<sup>c</sup>

<sup>a</sup>AAO-Macquarie, 105 Delhi Rd, North Ryde NSW 2113, Australia

<sup>b</sup>Department of Physics and Astronomy, Macquarie University, Sydney NSW 2109, Australia

<sup>c</sup>AAO-Stromlo/AITC, Australian National University, Cotter Road, Weston Creek, ACT 2611, Australia

<sup>d</sup>INAF, Viale del Parco Mellini, 84, 00136 Roma RM, Italy

<sup>e</sup>Laboratoire d'Astrophysique de Marseille, 38 Rue Frédéric Joliot Curie, 13013 Marseille, France

<sup>f</sup>European Southern Observatory, Karl-Schwarzschild-Straße 2, 85748 Garching bei München, Germany

<sup>g</sup>Observatoire de Paris, LESIA, 5 Place Jules Janssen, 92190 MEUDON, France

<sup>h</sup>ONERA, 29 avenue de la division Leclerc, 92320 CHATILLON, France

## ABSTRACT

The MCAO Assisted Visible Imager and Spectrograph (MAVIS) is a facility-grade visible MCAO instrument, currently under development for the Adaptive Optics Facility at the VLT. The adaptive optics system will feed both an imager and an integral field spectrograph, with unprecedented sky coverage of 50% at the Galactic Pole. The imager will deliver diffraction-limited image quality in the V band, cover a  $30'' \times 30''$  field of view, with imaging from U to z bands. The conceptual design for the spectrograph has a selectable field-of-view of  $2.5'' \times 3.6''$ , or  $5'' \times 7.2''$ , with a spatial sampling of 25 or 50 mas respectively. It will deliver a spectral resolving power of  $R=5,000$  to  $R=15,000$ , covering a wavelength range from 380 - 950 nm. The combined angular resolution and sensitivity of MAVIS fill a unique parameter space at optical wavelengths, that is highly complementary to that of future next-generation facilities like JWST and ELTs, optimised for infrared wavelengths. MAVIS will facilitate a broad range of science, including monitoring solar system bodies in support of space missions; resolving protoplanetary- and accretion-disk mechanisms around stars; combining radial velocities and proper motions to detect intermediate-mass black holes; characterising resolved stellar populations in galaxies beyond the local group; resolving galaxies spectrally and spatially on parsec scales out to 50 Mpc; tracing the role of star clusters across cosmic time; and characterising the first globular clusters in formation via gravitational lensing. We describe the science cases and the concept designs for the imager and spectrograph.

---

Further author information: (Send correspondence to S.C.E.)

S.C.E.: E-mail: simon.ellis@mq.edu.au, Telephone: +61 2 9372 4845

**Keywords:** Multi-conjugate adaptive optics, Imagers, Integral field spectrographs, Spectrographs, Adaptive optics, Image slicers

## 1. INTRODUCTION

Historically astronomical adaptive optics was first applied over small fields-of-view and at near-infrared wavelengths.<sup>1</sup> This is naturally the case since Fried’s parameter, i.e. the diameter of a bundle of rays which remain in phase when passing through the atmosphere, has a wavelength dependence of  $r_0 \propto \lambda^{\frac{6}{5}}$ . Therefore correcting over larger fields and at shorter wavelengths is more difficult, because there will be a greater variation in the phase of the wavefront across the telescope pupil. In fact, due to the advances made in AO it is now possible to correct over large fields-of-view of 90 – 120 arcmin, using multi-conjugate AO (MCAO), as has been demonstrated with MAD<sup>2,3</sup> on the VLT using natural guide stars (NGS) and with GeMS<sup>4,5</sup> on Gemini using laser guide stars (LGS). It is also possible to perform AO at visible wavelengths, as has been demonstrated with MagAO<sup>6</sup> at Magellan.

MAVIS, the MCAO Assisted Visible Imager and Spectrograph, will combine these advances allowing wide-field MCAO corrected observations in the visible for the first time. MAVIS will operate on the adaptive optics facility of UT4 at the VLT, and is currently in the preliminary design phase. MAVIS consists of three modules, the adaptive optics model (AOM), an imager, and an integral field spectrograph (IFS). An overview of the MAVIS instrument as a whole can be found in 7, and the instrument and the individual modules and predicted performance are described in a series of papers within this conference.<sup>8-17</sup> A summary of the main parameters of the AOM are given in Table 1. Note in particular, that the use of 8 LGS allows an MCAO corrected field-of-view of 30” diameter with diffraction limited imaging at 550 nm with a Strehl of  $\geq 10\%$ ; and the use of up to 3 NGS allows an unprecedented sky coverage of  $> 50\%$  at the Galactic pole.

Table 1. MAVIS adaptive optics module main parameters

Focus	Nasmyth A VLT-AOF UT4
Corrected field-of-view	30” diameter
Sky coverage	$\geq 50\%$ at Galactic pole
Strehl ratio	$\geq 10\%$ in V (goal 15%), $< 10\%$ variation (RMS)
Ensquared energy	$\geq 15\%$ within 50 mas at 550 nm
NGS field-of-view	120” diameter
Number of NGS	up to 3
Limiting magnitude	$H \geq 18.5$ mag
Number of LGS	8

This paper describes the conceptual design of the two science instruments. The key instrument parameters are given in Table 2 and 3. We begin with a summary of the MAVIS science cases, followed by a description of the concept design of the imager and the spectrograph. We conclude with a summary of the present status of the instruments and an outline of future work.

Table 2. MAVIS imager parameters

Field of View	30.2” $\times$ 29.5”
Pixel Scale	7.36 mas/pix
Sensitivity	V $> 29$ mag ( $5\sigma$ ) in 1hr
Filters	7 broad-band, 15 narrow-band filters

Table 3. MAVIS spectrograph parameters

Spatial sampling mode	Spaxel size (mas)	Field-of-view (arcsec)	
Fine sampling	20 – 25	$2.5'' \times 3.6''$	
Coarse sampling	40 – 50	$5.0'' \times 7.2''$	
Spectral mode	Median resolving power	Wavelength range (nm)	$10\sigma$ limiting mag in 1hr (AB mag; fine sampling mode)
LR-Blue	5900	370 – 720	21.0 @ 550 nm
LR-Red	5900	510 – 1000	21.5 @ 740 nm
HR-Blue	14700	425 – 550	19.6 @ 475 nm
HR-Red	11500	630 – 880	20.7 @ 725 nm

## 2. SCIENCE CASES

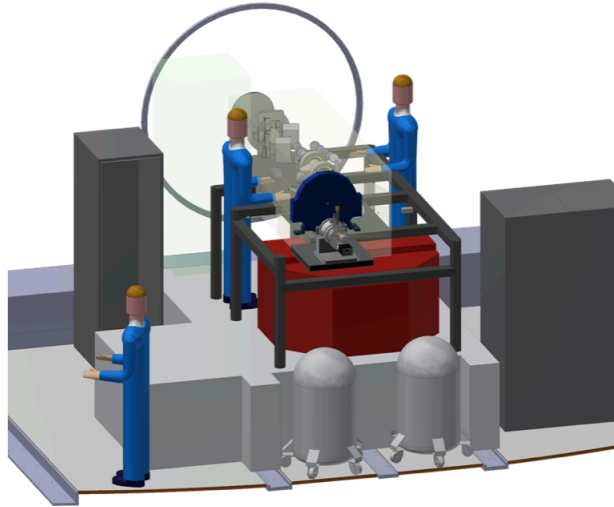
The MAVIS science cases are described in detail in Ref. 18; here we give a brief overview. The MAVIS science cases exploit the unique capabilities of the instrument. MAVIS will deliver the finest angular resolution at visible wavelengths of any single optical telescope available in the next decade, either ground-based or space-based, including the JWST and the next generation of ELTs. This will allow the deepest ever detections of point sources and compact galaxies at visible wavelengths, with  $I \approx 30.4$  mag in 10 hr, cf.  $I = 29.4$  mag in 100 hr for the Hubble Ultra Deep Field. Furthermore, the sky coverage of  $> 50\%$  even within 10 deg of the Galactic pole, allows this performance in a truly general purpose instrument. The resolution at V of  $\approx 18$  mas is similar to the NIR resolution of the ELT (e.g. 14 mas in K for MICADO<sup>19</sup>); MAVIS will allow continued access to the full UV-NIR wavelength range at the highest spatial resolution, which would otherwise be impossible in the post HST-era. Moreover, the visible wavelength range contains key diagnostic features which will be unavailable to ELTs at this resolution.

This performance is accessible to imaging over  $30 \times 30$  arcsec from U – I bands, astrometry with a precision of  $150 \mu\text{as}$ , and integral field spectroscopy at  $25 - 50$  mas sampling over  $\approx 9$  arcsec<sup>2</sup>. MAVIS is thus a general purpose facility instrument, and can address a broad range of science cases. The consortium have compiled a range of white papers in consultation with the ESO community. These have been classified under four themes, as will be briefly summarised below. For full details we again refer the reader to Ref. 18.

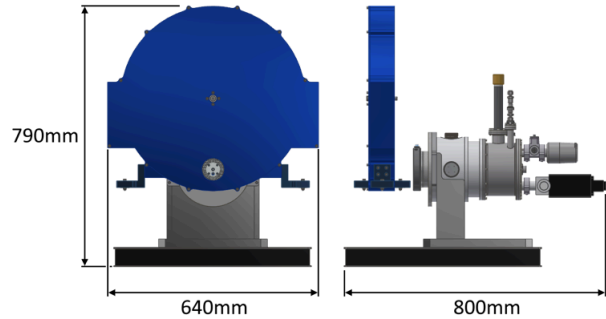
The first theme is ‘The emergence of the Hubble sequence’. Galaxies in the early Universe show a clumpy and disordered morphology, combined with a very high gas velocity dispersions in a rotationally dominated systems. These turbulent, clumpy discs somehow evolve into the present day Hubble sequence via a rapid decline in star-formation and gas content around  $z \sim 1$ . MAVIS will exploit its high spatial resolution and spectroscopic capabilities to measure the morphology, kinematics and spatially resolved ISM properties during this crucial epoch of galaxy evolution.

The second theme is ‘Resolving the contents of galaxies beyond the local group’. Current astrometric, photometric and spectroscopic surveys (e.g. GAIA, GALAH, APOGEE, 4MOST, SDSS-V Galactic Genesis Survey) will map both the disc and bulge of the Milky Way, measuring stellar ages, chemistry and kinematics, as well as the composition and dynamics of gas and dust in star-forming regions. To place these findings in context it is necessary to extend such measurements to other galaxies. MAVIS will allow imaging on  $< 2$  pc pixel scales, and spectroscopy on  $< 5 - 10$  pc spaxel scales out to 50 Mpc, allowing the measurement of detailed ‘sub-grid’ physics well beyond the local group.

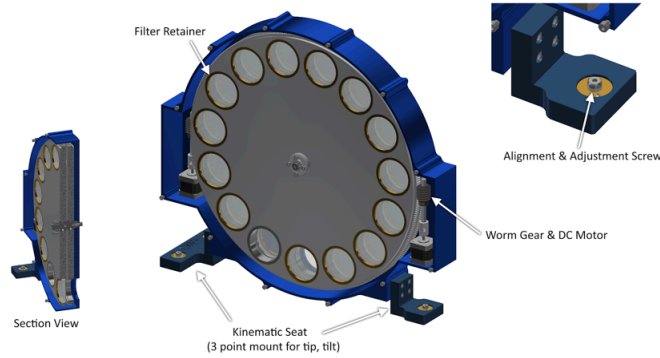
The third theme is ‘Star clusters over cosmic time’. The high spatial resolution of MAVIS will allow spatially resolved imaging and spectroscopy in the crowded regions of star-clusters at different times and spatial scales, connecting together the physics driving star-formation, and stellar and galactic evolution. For example, MAVIS will allow us to connect stellar clusters at different redshifts, and to understand the fate of high redshift clump, to understand the origin of multiple populations in clusters, to search for intermediate mass black holes in clusters, and to understand the role of metallicity in the evolution of massive stars.



(a) The imager on the Nasmyth platform



(b) Dimensions of the imager



(c) Filter wheels

Figure 1. Schematic drawings of the imager concept

The fourth theme is ‘The birth, life and death of stars and their planets’. MAVIS will provide the resolution to investigate the immediate environments of individual nearby stars, for example measuring the evolution of proto-planetary discs, the formation of jets and the removal of angular momentum, and the nature of white dwarf merger systems. In addition, in our own solar system, MAVIS will allow the characterisation of the three dimensional structure of planetary atmospheres, the measurement of the surface and atmospheric composition of comets, rings and planets, and the monitoring of faint solar system bodies.

### 3. IMAGER

The AOM feeds both science instruments with a telecentric ( $< 1$  deg non-telecentricity), flat (ROC= 1200 mm),  $f/35.0$  beam, see Ref.<sup>10</sup> for full details. This provides a plate-scale of 0.736 arcsec/mm, and the imager takes this input and images it directly onto the detector with no-relay optics, other than the filters. Figure 1 shows schematic drawings of the imager concept.

The baseline image sensor is the CCD250 from Teledyne e2v. This sensor has  $4096 \times 4004$  pixels with a size of  $10 \mu\text{m}$ , leading to a pixel size of 7.36 mas, and a field-of-view of  $30.2 \times 29.5$  arcsec. The pixel size is chosen to sample properly the diffraction limit at 550 nm. The FWHM of a diffraction limited Airy pattern at 550 nm is 14.18 mas for an 8 m telescope, but in fact the effective PSF will be larger than this due to the effects of

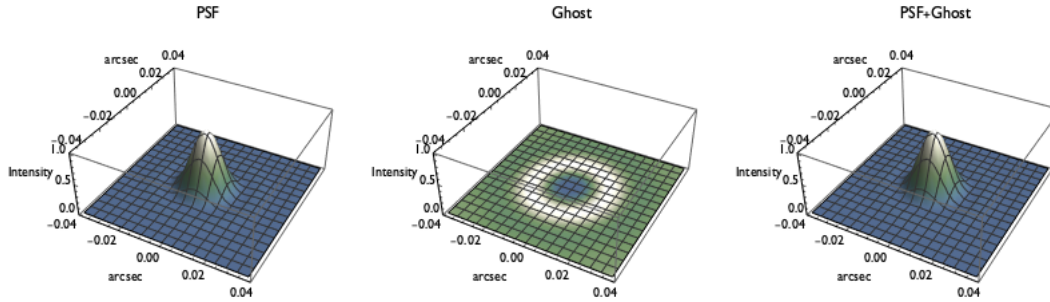


Figure 2. The second order ghosts produced from two internal reflections of 2% each in the filter, compared to the PSF without ghosts.

charge diffusion within the CCD (whereby some fraction of photoelectrons are collected in adjacent pixels due to scattering as the electrons move towards the pixel), and also residual tip-tilt errors. The CCD250 has a charge diffusion of  $< 4 \mu\text{m}$  at 550 nm, or 0.94 pixels, and the tip-tilt residual is  $\sim 8.5 \text{ mas}$  or 1.15 pixels. Thus the effective PSF at 550 nm is 17.9 mas, which is sampled by 2.43 pixels, such that we will still be well sampled in good conditions.

The imager will have two filter wheels in series, each with 15 positions. The first will contain 7 broadband filters, 7 narrow-band filters, and 1 clear aperture; the second wheel will contain 5 neutral density filters with OD 1- 5, 8 narrow-band filters, and 1 clear aperture.

The filters will be in a converging beam, albeit a slow beam at  $f/35$ . Therefore, tilting the filters to avoid ghosts from secondary reflections would lead to both lateral spherical aberration and lateral astigmatism. The astigmatism is significant compared to the diffraction limited PSF; a 5 deg tilt leads to an astigmatism of 25 mas, and any tilt larger than 0.38 deg leads to astigmatism larger than the desired astrometric precision of  $150 \mu\text{as}$ . Therefore we adopt an approach of having no tilt on the filters. This means that ghosts will now overlap directly with the images. Figure 2 shows the second order ghosts produced from two internal reflections of 2% each in the filter, compared to the PSF without ghosts. The ghosts change the integrated intensity in a Gaussian fit to the PSF by one part in  $10^6$  and the FWHM by 3 parts in  $10^6$ . This analysis does not include the effects of residual wavefront errors in the PSF, nor does it include any other ghosts; these will be included in future analyses. Nevertheless, it shows that the ghosts are not significant at the concept design level. The shift in filter bandpass due to the converging beam is negligible.

In order to achieve a relative astrometric precision of  $150 \mu\text{as}$  over the field, the filters must be very flat, otherwise distortions would be introduced which could be hard to calibrate. The filters are 75 mm in diameter, for which the standard thickness is 12.5 mm. To keep the radial distortions introduced by the filter  $< 0.7 \text{ mas}$  (assuming that the final precision can be improved by a factor  $\sim 10$  through calibration), then we require a filter flatness of  $\lambda/2$  peak-to-valley, over the 75 mm aperture of the filter, or  $\lambda/8.5$  RMS. These are all within standard “high precision” specifications for filter flatnesses, but can be eased if the filters are placed closer to the detector.

#### 4. SPECTROGRAPH

MAVIS will have an integral field spectrograph, with the main parameters as listed in Table 3. The spectrograph will be selected via a deployable fold-mirror, and will accept the same  $f/35.0$  input beam from the AOM as the imager.

The spectrograph has two spatial sampling modes. In the first mode it will have 25 mas spaxels with a  $3.6'' \times 2.5''$  field-of-view, and in the second it will have 50 mas spaxels with a  $7.2'' \times 5.0''$  field-of-view. The sampling is chosen as a compromise between resolution and sensitivity to low surface brightness objects. The field-of-view will be offset from the centre of the imager field-of-view by  $\approx 10 \text{ arcsec}$  such that it can be rotated to sweep out an annulus of accessible sky for any given NGS asterism.

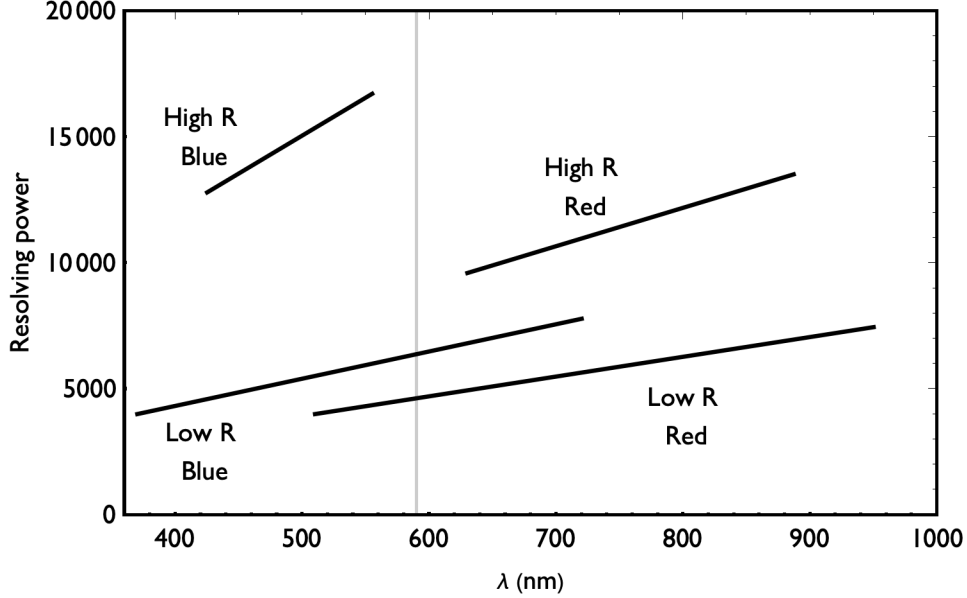


Figure 3. The resolving power and wavelength range of each of the spectrograph spectral modes; see also Table 3.

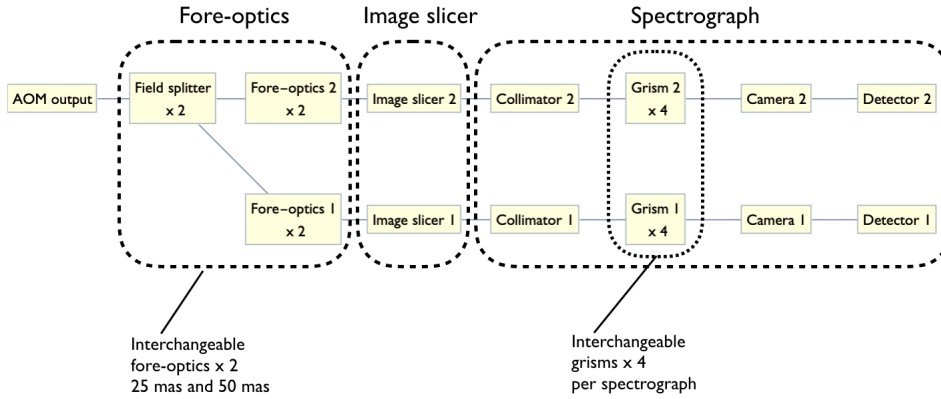


Figure 4. Block diagram of the main spectrograph components. The field is first split in two, after which there are two identical arms consisting of fore-optics, image slicer and spectrograph.

The spectrograph has four spectral resolution modes, with resolving power and wavelength coverage as listed in Table 3 and shown in Figure 3. These modes support a wide range of science cases as described in Ref.,<sup>18</sup> and summarised in section 2.

The spectrograph consists of three sub-modules: the fore-optics which splits the field into two and magnifies the beam onto the IFU, an image slicing IFU, and the spectrograph proper. Following the field-splitter there are two identical arms, as shown in Figure 4. We now describe each of these components in turn.

The optical design of the field-splitter and image slicer are described in detail in a companion paper,<sup>14</sup> here we give a summary. Figure 5 shows the optomechanical design. A 90 deg mirror splits the field-of-view into two along the long axis. Two toroidal mirrors then provide an anamorphic magnification of the beam onto the image slicer. The anamorphism is such that the focal ratio is halved in the spatial direction, and at the detector the PSF is sampled by one pixel in the spatial direction and two pixels in the spectral direction. These mirrors are interchangeable with another set to provide either the 25 mas or 50 mas modes.

An image is then formed on the first mirror stack, which slices the field into 50 slices of  $3.2'' \times 25$  mas or  $7.6'' \times 50$  mas depending on the fore-optics. These mirrors form a pupil image on a second stack of mirrors.

These are designed to accept the full pupil for the 50 mas mode and are underfilled in the 25 mas mode. These mirrors reform an image on the spectrograph entrance slit via a final fold mirror to redirect the light.

Following the image slicer are the two spectrographs proper. There are two identical spectrographs in order to achieve the full field-of-view. The optical design of the spectrograph is shown in Figure 6. The physical size of the spectrograph slit is the same in all modes, and is fed at different focal ratios depending on the mode, as listed in Table 4

Table 4. MAVIS spectrograph slit parameter

	25 mas		50 mas	
	Spectral direction	Spatial direction	Spectral direction	Spatial direction
Focal ratio	40	20	20	10
Angular size	25 mas	3.6 arcsec	50 mas	7.2 arcsec
Physical size	39 $\mu\text{m}$	164 mm	39 $\mu\text{m}$	164 mm

The spectrograph optics are designed for a sampling of 2.3 pixels per resolution element. The image sensor is the Teledyne e2v CCD290-99 device with 9k $\times$ 9k 10  $\mu\text{m}$  pixels. The spectrograph uses a collimator with 483 mm focal length, maintaining the natural pupil size generated by the image slicer optics. Because of the operation in different modes, chromatic aberration cannot be compensated for by detector tilt, the optics are therefore corrected over the full wavelength range of 370 – 1000 nm. In addition, the collimator is optimized separately from the spectrograph camera, to avoid generating higher order aberrations in the grism assemblies; this also helps in testing both assemblies independently. The design uses glasses selected from the i-Line catalogs of Nikon, Ohara and Schott, as well as other high transmission glass from those vendors, for high transmission down to 370 nm, and to ensure availability. The detector cryostat window is fused silica to avoid an enhanced background on the CCD due to radioactivity in the glass. The cryostat window has optical power and is integral to the camera design. Both the collimator and the camera design require some mild aspherical surfaces, with two surfaces in the collimator and one in the camera.

To enhance throughput, and simplify the mechanical design of the lens barrels, the lenses are arranged in cemented groups where practical. The lens diameters in the cemented groups are between 70 mm and 139 mm, and the internal radii and CTE differences present no problem for cementing. The largest lens diameter is 164 mm (penultimate lens, just before the cryostat window). The choice of high transmission glasses leads to a transmission (glass bulk absorption and surface reflections) of > 77% average. The design contains 22 glass-air surfaces (excluding the grisms); we assume average losses of 1% per surface as a baseline, and are investigating coating options to improve this number.

The theoretical image quality of the design is shown in Figure 7, which shows the ‘enslitted’ energy as a function of position on the detector for each spectral mode. Overlaid are spot diagrams of the PSF at the same position. The wavelength at the given position is shown by the numbers on the right hand side of the plots. These results are summarised in Table 5. The overall throughput from field-splitter to CCD for each mode is shown in Figure 8.

Table 5. The ‘enslitted’ energy for each spectrograph mode

	25 mas			50 mas		
	Min	Max	Mean	Min	Max	Mean
LR Blue	0.79	0.90	0.86	0.76	0.94	0.88
HR Blue	0.77	0.87	0.82	0.80	0.92	0.86
LR Red	0.85	0.89	0.87	0.84	0.94	0.89
HR Red	0.78	0.84	0.82	0.79	0.90	0.85

The optomechanical design is shown in Figure 9. The overall construction of the spectrograph is out of aluminium and the size is such that both the spectrographs would fit entirely on an optical table. The material

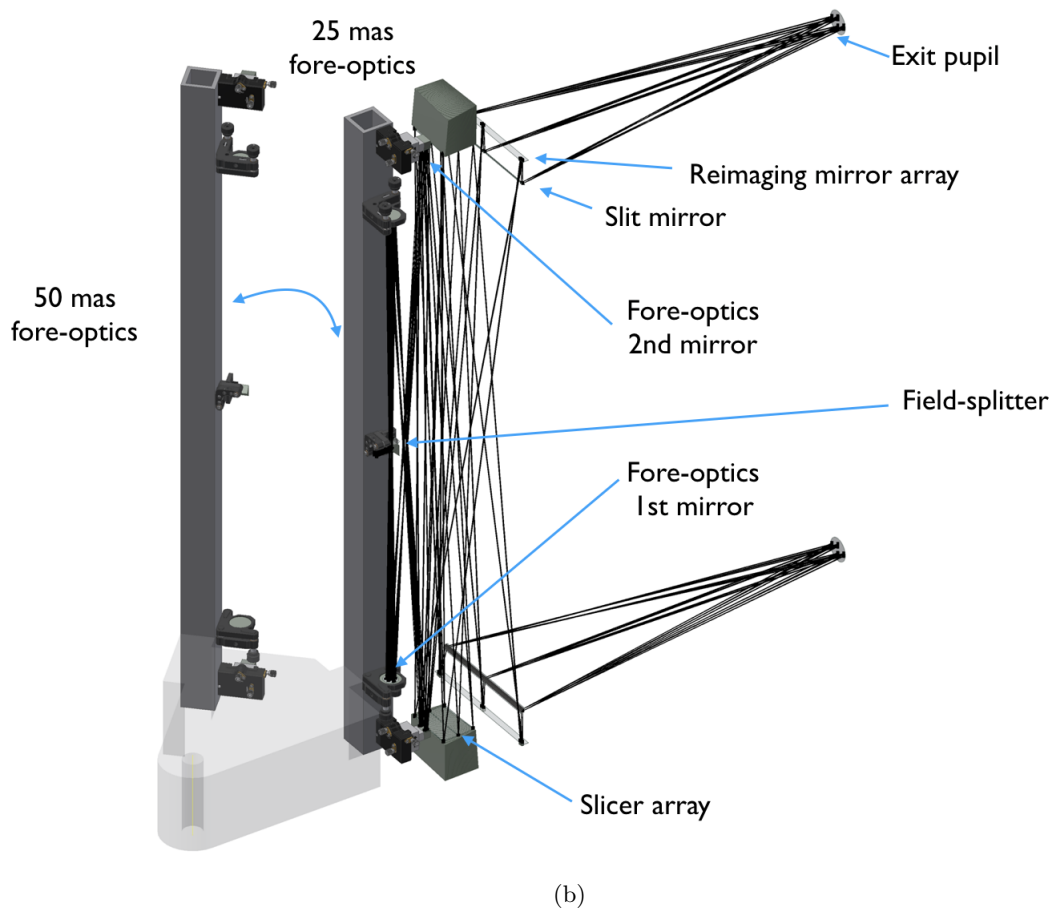
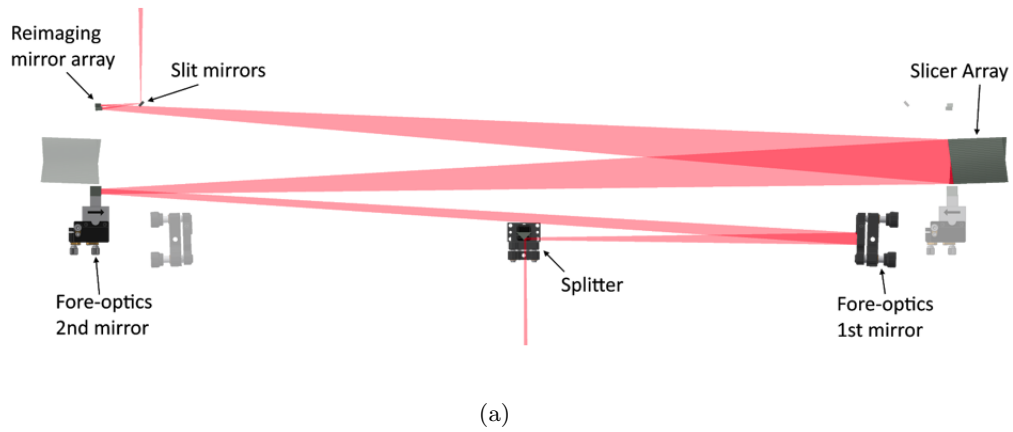


Figure 5. Optomechanical design of the fore-optics and image slicer. The top figure shows a plan view of the system from above, with the light path traced out for one arm only. The bottom figure shows both arms, as well as the exchange mechanism for the fore-optics. See Ref.<sup>14</sup> for details on the optical design

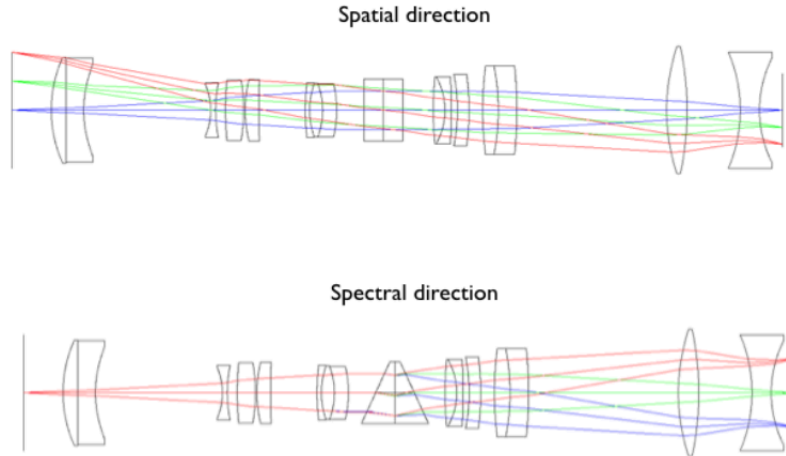


Figure 6. Optical design of the spectrographs. Spectrograph optical design in the 50 mas mode. The collimator is on the left hand side and produces a  $\sim 50$  mm pupil. The total length from input slit to detector plane is 1020 mm. The interchangeable grism assemblies in the pupil work without beam deflection and enable different modes without moving any other optics.

for the spectrograph base-plate is MIC-6 cast plate which sets the foundation to mount the collimator, camera and cryostat assemblies. The structure will have a profile machined to set the position of each assembly. The material for the collimator and camera assemblies is aluminium. Each lens is mounted in an individual cell with the optical surface resting on a tangential cell surface. An RTV bond will be applied to the perimeter of the lens cell and axial retention ring will be threaded into place. Each lens sub-assembly will be potted and aligned coaxially and then screwed to complete lens assembly. The spectrograph assembly consists of a main structural frame. The structural frame will house the two spectrographs, image slicer, field splitter, mounted side-by-side, with both image slicers mounted kinematically on the main structural frame to feed each spectrograph. This main structural frame will interface with the MAVIS Overall Mechanical System. Each spectrograph will be mounted on a sliding frame to provide easy access for installation, commissioning and maintenance. The position of the spectrograph on the Nasmyth platform in relation to the rest of the instrument is shown in Figure 10.

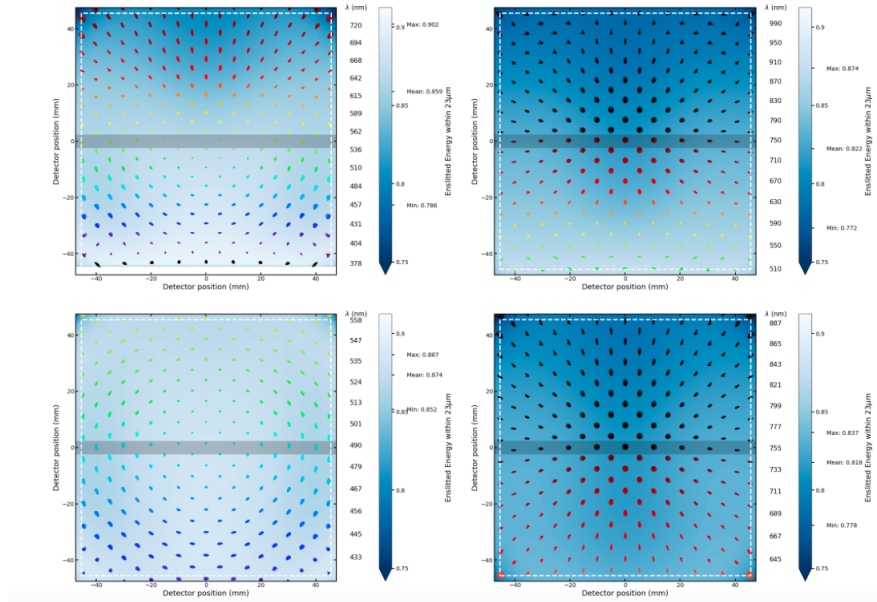
## 5. SUMMARY

We have described the science case and conceptual design for the MAVIS science instruments. The combination of an MCAO assisted visible imager and integral field spectrograph, operating at the frontier of angular resolution and sensitivity will provide access to a unique parameter space, enabling a broad range of science cases from solar-system objects to the early Universe.

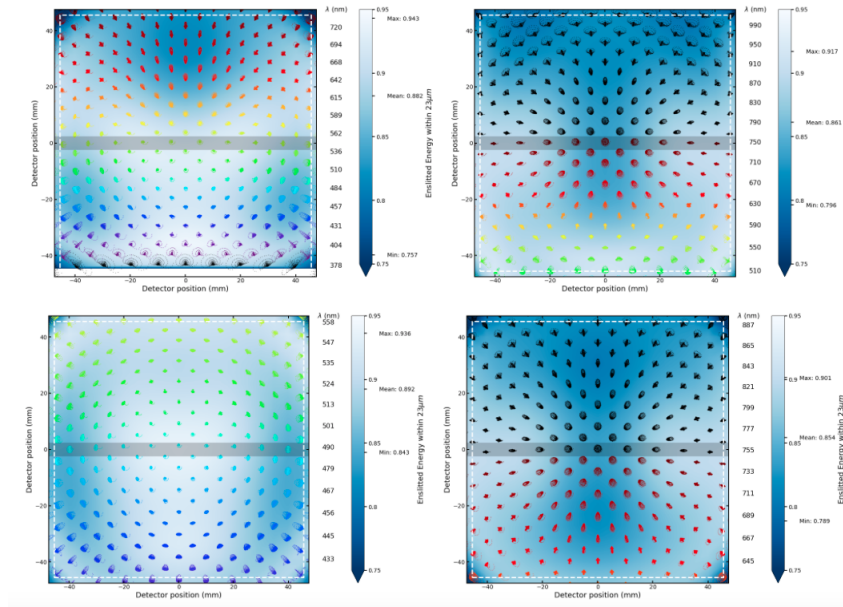
The ESO Phase A review of MAVIS was successful, and approval for construction is currently following the regular process through the Science and Technical Committee, and the Finance Committee and Council at ESO. During Phase B we will complete the preliminary design of the instruments, complete further trade-off studies, costings, and identify risks. In particular we will examine trade-offs in the imager detectors, the impact of ghsots on the imager, and the spectrograph slicer design, which is a critical and expensive component of the instrument. We will further optimise the design of spectrograph including the effects of diffraction which are important in an AO corrected instrument working near the diffraction limit.

## REFERENCES

- [1] Rousset, G., Fontanella, J. C., Kern, P., Gigan, P., and Rigaut, F., “First diffraction-limited astronomical images with adaptive optics,” *A&A* **230**, L29–L32 (Apr. 1990).



(a) 25 mas



(b) 50 mas

Figure 7. The ‘enslitted’ energy as a function of position on the detector for the spectrograph for the 25 mas mode (panel a) and the 50 mas mode (panel b). The top row is for the low resolution settings and the bottom row for the high resolution settings. The images in the left hand column are for the blue settings, and the ones in the right hand column are for the red settings. Overlaid are the PSFs at the detector position. The wavelengths are shown at the right hand side of each plot. These numbers take into account the actual width of the slit, convolved with the local Huygens PSF to derive the amount of energy recorded in a resolution element that is 2.3 pixels wide, corresponding to the nominal width of the slit image.

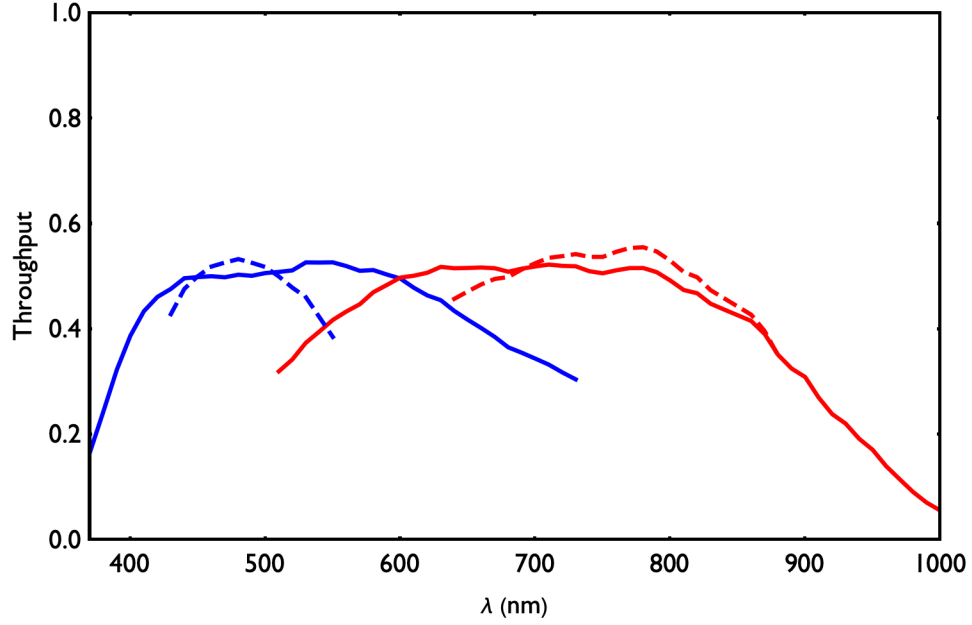


Figure 8. The estimated throughput of the spectrograph from field-splitter to CCD. The dashed curves are for the high resolution modes, and the continuous curves are for the low resolution settings.

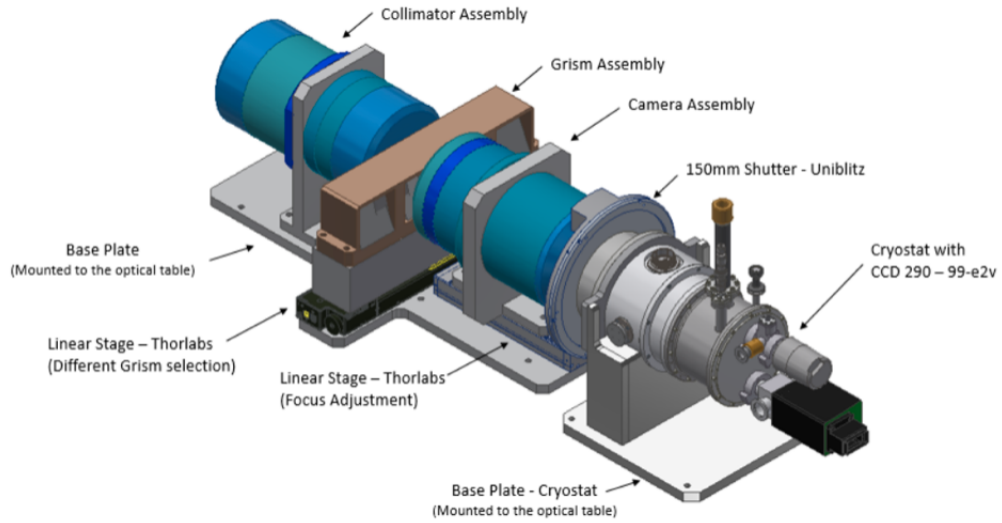


Figure 9. 3D model of the mechanical design and layout of the spectrograph sub-module. There will be four independent settings for the spectrograph providing different spectral resolution and wavelength ranges. These settings can be exchanged by different gratings mounted on a linear stage as shown above.

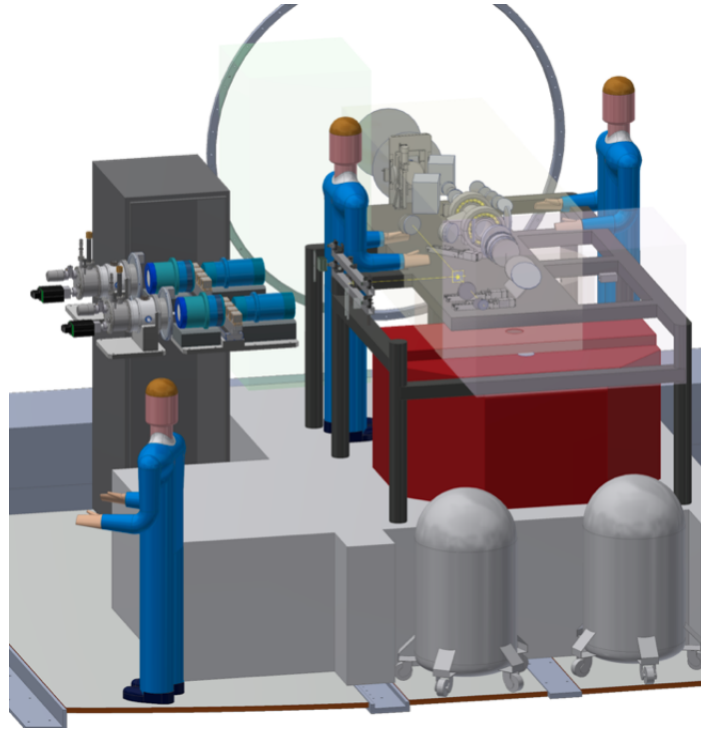


Figure 10. The approximate location of the spectrograph on the Nasmyth platform.

- [2] Marchetti, E., Hubin, N. N., Fedrigo, E., Brynnel, J., Delabre, B., Donaldson, R., Franza, F., Conan, R., Le Louarn, M., Cavadore, C., Balestra, A., Baade, D., Lizon, J.-L., Gilmozzi, R., Monnet, G. J., Ragazzoni, R., Arcidiacono, C., Baruffolo, A., Diolaiti, E., Farinato, J., Vernet-Viard, E., Butler, D. J., Hippler, S., and Amorin, A., “MAD the ESO multi-conjugate adaptive optics demonstrator,” *Proc. SPIE* **4839**, 317–328 (Feb. 2003).
- [3] Marchetti, E., Brast, R., Delabre, B., Donaldson, R., Fedrigo, E., Frank, C., Hubin, N., Kolb, J., Lizon, J.-L., Marchesi, M., Oberti, S., Reiss, R., Soenke, C., Tordo, S., Baruffolo, A., Bagnara, P., Amorim, A., and Lima, J., “MAD on sky results in star oriented mode,” *Proc. SPIE* **7015**, 70150F (July 2008).
- [4] Rigaut, F., Neichel, B., Boccas, M., D’Orgeville, C., Vidal, F., van Dam, M. A., Arriagada, G., Fesquet, V., Galvez, R. L., Gausachs, G., Cavedoni, C., Ebbers, A. W., Karewicz, S., James, E., Lührs, J., Montes, V., Perez, G., Rambold, W. N., Rojas, R., Walker, S., Bec, M., Trancho, G., Sheehan, M., Irarrazaval, B., Boyer, C., Ellerbroek, B. L., Flicker, R., Gratadour, D., Garcia-Rissmann, A., and Daruich, F., “Gemini multiconjugate adaptive optics system review - I. Design, trade-offs and integration,” *MNRAS* **437**, 2361–2375 (Jan. 2014).
- [5] Neichel, B., Rigaut, F., Vidal, F., van Dam, M. A., Garrel, V., Carrasco, E. R., Pessev, P., Winge, C., Boccas, M., D’Orgeville, C., Arriagada, G., Serio, A., Fesquet, V., Rambold, W. N., Lührs, J., Moreno, C., Gausachs, G., Galvez, R. L., Montes, V., Vucina, T. B., Marin, E., Urrutia, C., Lopez, A., Diggs, S. J., Marchant, C., Ebbers, A. W., Trujillo, C., Bec, M., Trancho, G., McGregor, P., Young, P. J., Colazo, F., and Edwards, M. L., “Gemini multiconjugate adaptive optics system review - II. Commissioning, operation and overall performance,” *MNRAS* **440**, 1002–1019 (May 2014).
- [6] Close, L. M., Males, J. R., Morzinski, K., Kopon, D., Follette, K., Rodigas, T. J., Hinz, P., Wu, Y. L., Puglisi, A., Esposito, S., Riccardi, A., Pinna, E., Xompero, M., Briguglio, R., Uomoto, A., and Hare, T., “Diffraction-limited Visible Light Images of Orion Trapezium Cluster with the Magellan Adaptive Secondary Adaptive Optics System (MagAO),” *Astrophys. J.* **774**, 94 (Sept. 2013).
- [7] Rigaut, F., McDermid, R., Cresci, G., Viotto, V., Ellis, S., Broderick, D., Agapito, G., Fusco, T., Neichel, B., Haguenaer, P., Plantet, C., Salasnich, B., Aliverti, M., Antonucci, S., Balestra, A., Baruffolo, A., Bergomi, M., Bonaglia, M., Bono, G., Busoni, L., Carolo, E., Chinellato, S., Content, R., Cranney, J., De

Silva, G., Esposito, S., Fantinel, D., Farinato, J., Haynes, D., Horton, A., Gaston, G., Gilbert, J., Gratadour, D., Greggio, D., Gullieuszik, M., Korhikoski, V., Magrin, D., Magrini, L., Marafatto, L., Mcgregor, H., Mendel, T., Monty, S., Pedichini, F., Pinna, E., Portaluri, E., Radhakrishnan, K., Ragazzoni, R., Robertson, D., Schwab, C., Sharp, R., Stroebele, S., Thorn, E., Vaccarella, A., Vassallo, D., Venkatesan, S., Waller, L., Warner, S., Zamkotsian, F., and Zhang, H., “MAVIS conceptual design,” in [(submitted to) *Ground-based and Airborne Instrumentation for Astronomy VIII*], International Society for Optics and Photonics, SPIE (2020).

- [8] Agapito, G., Vassallo, D., Plantet, C., V.Viotto, and et al, E. P., “MAVIS: System modelling and performance prediction,” *Proc. SPIE 11448 (this conference)* (2020).
- [9] Salasnich, B., Baruffolo, A., Balestra, A., and Fantinel, D., “MAVIS: Conceptual architecture of the instrument control software,” *Proc. SPIE 11448-105 (this conference)* (2020).
- [10] Greggio, D., Filippo, S. D., Magrin, D., Schwab, C., and et al, V. V., “MAVIS adaptive optics module optical design,” *Proc. SPIE 11448-280 (this conference)* (2020).
- [11] Gratadour, D., Bernard, J., Doucet, N., Ferreira, F., Sevin, A., Biasi, R., and Rigaut, F., “MAVIS Real-Time Control system: a high-end implementation of the COSMIC platform,” *Proc. SPIE 11448-144 (this conference)* (2020).
- [12] Monty, S., McDermid, R., Rigaut, F., Taheri, M., Agapito, G., and et al, “The MAVIS image simulator: predicting the astrometric performance and sensitivity of MAVIS,” *Proc. SPIE 11448-265 (this conference)* (2020).
- [13] Viotto, V., Pinna, E., Agapito, G., Aliverti, M., Arcidiacono, C., and et al, “MAVIS: The Adaptive Optics Module feasibility study,” *Proc. SPIE 11448-9 (this conference)* (2020).
- [14] Content, R., Ellis, S., Schwab, C., Rigaut, F., McDermid, R., and Cresci, C., “MAVIS: Image slicer concept and design,” *Proc. SPIE 11451-266 (this conference)* (2020).
- [15] Cranney, J., Zhang, H., Gratadour, D., Rigaut, F., Korhikoski, V., and et al, “MAVIS predictive control in learn and apply framework,” *Proc. SPIE 11448-143 (this conference)* (2020).
- [16] Zhang, H., Cranney, J., Doucet, N., Korhikoski, V., Gratadour, D., and Rigaut, F., “MAVIS learn and apply application and performance analysis,” *Proc. SPIE 11448-93 (this conference)* (2020).
- [17] Greggio, D., Schwab, C., Filippo, S. D., Magrin, D., Viotto, V., Pinna, E., and Rigaut, F., “Optical design of a broadband atmospheric dispersion corrector for MAVIS,” *Proc. SPIE 11448-263 (this conference)* (2020).
- [18] McDermid, R. M., Cresci, G., Rigaut, F., Bouret, J.-C., De Silva, G., Gullieuszik, M., Magrini, L., Mendel, J. T., Antonucci, S., Bono, G., Kamath, D., Monty, S., Baumgardt, H., Cortese, L., Fisher, D., Mannucci, F., Migliorini, A., Sweet, S., Vanzella, E., Zibetti, S., and White Papers., w. a. c. f. t. a. o. t. M., “Phase A Science Case for MAVIS – The Multi-conjugate Adaptive-optics Visible Imager-Spectrograph for the VLT Adaptive Optics Facility,” *arXiv e-prints*, arXiv:2009.09242 (Sept. 2020).
- [19] Davies, R., Alves, J., Clénet, Y., Lang-Bardl, F., Nicklas, H., Pott, J. U., Ragazzoni, R., Tolstoy, E., Amico, P., Anwand-Heerwart, H., Barboza, S., Barl, L., Baudoz, P., Bender, R., Bezawada, N., Bizenberger, P., Boland, W., Bonifacio, P., Borgo, B., Buey, T., Chapron, F., Chemla, F., Cohen, M., Czoske, O., Déo, V., Disseau, K., Dreizler, S., Dupuis, O., Fabricius, M., Falomo, R., Fedou, P., Förster Schreiber, N., Garrel, V., Geis, N., Gemperlein, H., Gendron, E., Genzel, R., Gillessen, S., Glück, M., Grupp, F., Hartl, M., Häuser, M., Hess, H. J., Hofferbert, R., Hopp, U., Hörmann, V., Hubert, Z., Huby, E., Huet, J. M., Hutterer, V., Ives, D., Janssen, A., Jellema, W., Kausch, W., Kerber, F., Kravcar, H., Le Ruyet, B., Leschinski, K., Mandla, C., Manhart, M., Massari, D., Mei, S., Merlin, F., Mohr, L., Monna, A., Muench, N., Müller, F., Musters, G., Navarro, R., Neumann, U., Neumayer, N., Niebsch, J., Plattner, M., Przybilla, N., Rabien, S., Ramlau, R., Ramos, J., Ramsay, S., Rhode, P., Richter, A., Richter, J., Rix, H. W., Rodeghiero, G., Rohloff, R. R., Rosensteiner, M., Rousset, G., Schlichter, J., Schubert, J., Sevin, A., Stuik, R., Sturm, E., Thomas, J., Tromp, N., Verdoes-Kleijn, G., Vidal, F., Wagner, R., Wegner, M., Zeilinger, W., Ziegler, J., Ziegler, B., and Zins, G., “The MICADO first light imager for the ELT: overview, operation, simulation,” *Proc. SPIE 10702*, 107021S (July 2018).